

ANALYSIS OF INFINITE STRUCTURE RESPONSE DUE TO MOVING WHEEL IN THE PRESENCE OF IRREGULARITIES VIA GREEN'S FUNCTIONS METHOD

Traian MAZILU

University *Politehnica* of Bucharest, Department of Railway Vehicles
E-mail: trmazilu@yahoo.com

In this paper, the Green's functions method is employed to study wheel-rail interaction due to a single wheel moving at constant speed along a slab track. The slab track is considered as an infinite structure of two Euler-Bernoulli beams which are continuous elastic supported by Winkler layers. Starting from the properties of track's Green functions, the track's Green matrix is assembled in order to simulate wheel/rail interaction for any time. The method allows the computing of the nonlinear wheel/rail contact and it is accurate and efficient. Both frequency-domain and time-domain analysis of wheel/rail interaction are performed and the wheel velocity and nonlinear wheel/rail contact influences are pointed out.

Key words: wheel/rail interaction, slab track, irregularities, Green's functions.

1. INTRODUCTION

This paper deals with the response of infinite structure consisting of two continuous linear elastic coupled Euler-Bernoulli beams subjected to a uniformly moving wheel. Such a problem is of importance for wheel/rail interaction field, concerning particular aspects as the rolling noise [1], [2], [3], and the wear of the rolling surfaces [4], [5].

Generally, the track structure is represented by two kinds of mechanical models: the continuous model with one or two layer supports and the periodical model with discrete supports [6]. The first model is appropriate for the slab track and the second model is used for the ballasted track. The relatively new slab track is applied for high-speed railway lines [7] and for urban railway environment [8]. Here, the infinite structure of the double Euler-Bernoulli beams represents the slab track system. Similar models can be found in [9], [10], [11], [12].

The irregularities of the rail are one of the common causes of the wheel/rail vertical vibration, either the ballasted track or slab track. The rail irregularities have the wavelength in the range of 0.03 m – 3 m, as it follows: long wave and rolling defects with the wavelength between 1 m and 3 m, long wavelength rail corrugation from 0.1 m to 1 m, and short wavelength corrugation which has the wavelength of 0.03 m – 0.1 m [13]. The irregularities are starting point for wheel/rail vibrations from 15 Hz to 3000 Hz.

Analysis of wheel/rail interaction can be treated in the frequency-domain or/and in the time-domain using either the model of a moving irregularity between a stationary wheel and rail, or the model of a moving wheel along the track. The frequency-domain analysis requires a mandatory linear model. In fact, the track structure has nonlinearities [14], [15] and the wheel/rail contact is non-linear as well, according to the Hertz theory. However, most papers consider the track as a linear structure because this assumption gives the results in a good agreement with experimental researches [16]. On the other hand, the nonlinear contact influences the level of the wheel/rail vibration in the middle and high frequency range, particularly and for this particular reason it will be accounted.

The track is an infinite structure and its model has to be truncated, especially when the time-domain analysis is performed. If the wheel passes beyond the central zone of the model, errors caused by the edge-approach effect occur. Thus, the length of the considered track for the accurate numerical simulation will be limited, due to the boundary conditions. Many practical solutions for this issue may be invoked: the Fourier

transform in a semi-analytical approach [10], the cutting and merging method [17], the equivalent parametric model [18], the Fourier-series approach [19] or the Green's functions method [20], [21], [22].

In this paper, starting from previous author's researches, the Green's functions method is developed for the particular case of a moving wheel on a slab track. The problem can be studied in static frame or moving frame, but the first solution will be preferred for simplicity reasons.

2. MECHANICAL MODEL AND GOVERNING EQUATIONS

The structure of the slab track is composed of a massive concrete slab, into which the rails are embedded by means of Corkelast. The concrete slab acts as an efficient barrier between the soil motion (Rayleigh waves) and the rails. In light of the assumption that both rails and wheels are symmetrically loaded, only half track and a wheel are required for modelling.

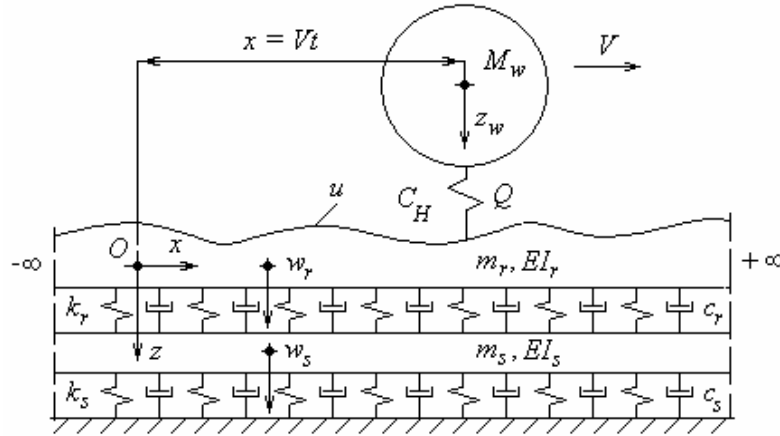


Fig. 2.1.

The mechanical model of a wheel moving at constant speed along a rail embedded in a slab track is depicted in fig. 2.1. Three subsystems can be identified: the wheel, the track and the wheel/rail contact.

The wheel is regarded as an M_w mass subjected to static load Q_0 and the normal contact force $Q(t)$, where t stands for time. This approach is frequently used when the natural frequencies of the vehicle suspension system are much lower than the ones of the wheel/rail vibration.

The slab track is reduced to a structure consisting of two Euler-Bernoulli beams coupled by Winkler foundation as the rail and the slab and the rail-pad, respectively.

The track is supported by the ground which is modelled as a Winkler foundation. The Euler-Bernoulli beam model is accurate enough as long as the cross-sectional dimensions are small compared to the bending wavelength [23].

The parameters for the two beams (index r for rail and index s for slab) are: the mass per length unit $m_{r,s}$ and the bending stiffness $EI_{r,s}$. The loss factor of the rail and the slab is neglected. The two Winkler foundations have the elastic constants $k_{r,s}$ per length unit and the viscous damping factors $c_{r,s}$ per length unit.

The vertical motion of the wheel is described by the equation

$$M_w \ddot{z}_w(t) = Q_0 - Q(t), \quad (2.1)$$

where $z_w(t)$ is the vertical displacement of the wheel.

Governing equations for the vertical forced vibrations of the track can be written as,

$$\mathbf{L}_{x,t} \{ \mathbf{w}(x,t) \} = \{ \mathbf{q}(t) \}, \quad (2.2)$$

where $\mathbf{L}_{x,t}$ stands for matrix differential

$$\mathbf{L}_{x,t} = \begin{bmatrix} EI_r \frac{\partial^4}{\partial x^4} + m_r \frac{\partial^2}{\partial t^2} + c_r \frac{\partial}{\partial t} + k_r & -c_r \frac{\partial}{\partial t} - k_r \\ -c_r \frac{\partial}{\partial t} - k_r & EI_s \frac{\partial^4}{\partial x^4} + m_s \frac{\partial^2}{\partial t^2} + (c_r + c_s) \frac{\partial}{\partial t} + (k_r + k_s) \end{bmatrix} \quad (2.3)$$

and $\{\mathbf{w}(x, t)\} = [w_r(x, t) \ w_s(x, t)]^T$ is the column vector of the rail and slab displacements, $\{\mathbf{q}(x, t)\} = [Q(t)\delta(x - Vt) \ 0]^T$ is the column vector of the vertical forces which act on the track, with $\delta(\cdot)$ is Dirac's delta function.

The boundary conditions are

$$\lim_{|x-Vt| \rightarrow \infty} \{\mathbf{w}(x, t)\} = [0 \ 0]^T, \quad (2.4)$$

and all initial conditions are set null, including the wheel displacement and the Q normal contact force.

The wheel/rail normal force is expressed according to the non-linear Hertz theory by

$$(Q(t)/C_H)^{2/3} = z_\delta(t)\sigma(z_\delta(t)), \quad (2.5)$$

where

$$z_\delta(t) = z_w(t) - w_r(Vt, t) - u(Vt), \quad (2.6)$$

is wheel/rail deflection, $u(Vt)$ is the rail roughness at the contact point, C_H represents the Hertzian constant and $\sigma(\cdot)$ is the Heaviside function. In fact, eq. (2.6) refers to the wheel/rail relative displacement in which the influence of wheel curvature has been neglected.

To solve the problem of the wheel/track interaction described by the preceding equations, the Green's functions method is proposed. For this aim, the real Green function's column vector for rail and slab displacement $\{\mathbf{g}(x, \xi, t - \tau)\} = [g_r(x, \xi, t - \tau), g_s(x, \xi, t - \tau)]^T$ is calculated starting from the complex Green functions of the track (the receptances). Basically, the real Green function's column vector $\{\mathbf{g}(x, \xi, t - \tau)\}$ contains the track's response in the x section at the $t - \tau$ moment, if at the τ moment in the ξ section along the rail an impulse force occurred and it verifies the equation

$$\mathbf{L}_{x,t} \{\mathbf{g}(x, \xi, t - \tau)\} = [\delta(x - \xi)\delta(t - \tau) \ 0]^T. \quad (2.7)$$

The complex Green function's column vector of the track represents the track response in the x section, caused by a unitary harmonic impulse force by an angular ω frequency, occurring in the ξ section of the rail

$$\{\mathbf{G}(x, \xi, \omega)\} = [G_r(x, \xi, \omega) \ G_s(x, \xi, \omega)]^T = F[\{\mathbf{g}(x, \xi, t)\}], \quad (2.8)$$

where $F[\cdot]$ stand for Fourier transform.

The track's complex Green functions are the solutions of the following equation

$$\mathbf{L}_{x,\omega} \{\mathbf{G}(x, \xi, \omega)\} = [\delta(x - \xi) \ 0]^T, \quad (2.9)$$

where $\mathbf{L}_{x,\omega}$ is the Fourier transform of the matrix operator $\mathbf{L}_{x,t}$. To find out $\{\mathbf{G}(x, \xi, \omega)\}$ vector, the previous equation is multiplied by the adjoint matrix operator $\mathbf{L}_{x,\omega}^*$, then eq. (2.9) yields

$$\text{diag}(H, H)\{\mathbf{G}(x, \xi, \omega)\} = \mathbf{L}_{x,\omega}^* [\delta(x - \xi) \ 0]^T, \quad (2.10)$$

with

$$H = a_0 \frac{d^8}{dx^8} + a_4 \frac{d^4}{dx^4} + a_8, \quad (2.11)$$

where $a_{0,4,8}$ are complex coefficients depending on the track's parameters and the angular frequency

$$a_0 = EI_r EI_s, \quad (2.12)$$

$$a_4 = EI_r [k_r + k_s - \omega^2 m_s + i\omega(c_r + c_s)] + EI_s (k_r - \omega^2 m_r + i\omega c_r),$$

$$a_8 = \omega^4 m_r m_s - i\omega^3 [m_r (c_r + c_s) + m_s] - \omega^2 [m_r (k_r + k_s) + m_s k_r + c_r c_s] + i\omega (k_r c_s + k_s c_r) + k_r k_s,$$

where $i^2 = -1$.

Practically, the complex Green functions may be obtained with the help of the Green function of H operator, named in the following as $\Gamma(x, x', \omega)$. This function verifies the equation

$$H\Gamma(x, x', \omega) = \delta(x - x') \quad (2.13)$$

and the boundary conditions

$$\lim_{x \rightarrow \pm\infty} \Gamma(x, x', \omega) = 0 \quad (2.14)$$

due to the track's damping.

As the solution of eq. (2.13), the Green function $\Gamma(x, x', \omega)$ can be obtained solving this equation by applying the Fourier transform from the space domain to the wave-number domain and then, using the inverse Fourier transform via the contour integration given by the theory of complex variables [12].

In this work, a different approach is undertaken; the starting point is the features of the Green function [24]. The Green function $\Gamma(x, x', \omega)$ is a linear combination of the functions $\exp(\lambda_i x)$ with $i = 1 \div 8$ corresponding to the solutions $\lambda_i = \lambda_i(\omega)$ of the characteristic equation of the H operator. It can be seen that if λ_i is one solution of the characteristic equation, then $-\lambda_i$ and $\pm i\lambda_i$ are solutions as well. Practically, each quadrant contains two solutions of the H operator characteristic equation.

According to the boundary conditions, the Green function of the H operator has the forms

$$\begin{aligned} \Gamma^-(x, x', \omega) &= \sum_{i=1}^4 A_i(x') \exp(\lambda_i x) \text{ for } -\infty < x < x', \\ \Gamma^+(x, x', \omega) &= \sum_{i=5}^8 A_i(x') \exp(\lambda_i x) \text{ for } x' < x < \infty, \end{aligned} \quad (2.15)$$

with $\text{Re}\lambda_i > 0$ for $i = 1 \div 4$ and $\text{Re}\lambda_i < 0$ for $i = 5 \div 8$.

On the other hand, the Green function is continuous in $x = x'$ and its first six derivatives are continuous as well

$$\Gamma^-(x', x', \omega) = \Gamma^+(x', x', \omega), \quad \frac{d^n \Gamma^-}{dx^n}(x', x', \omega) = \frac{d^n \Gamma^+}{dx^n}(x', x', \omega), \quad n = 1 \div 6. \quad (2.16)$$

Further on, the seventh derivative of the Green function has a discontinuity in $x = x'$

$$\frac{d^7 \Gamma^+}{dx^7}(x'+0, x', \omega) - \frac{d^7 \Gamma^-}{dx^7}(x'-0, x', \omega) = \frac{1}{a_0}. \quad (2.17)$$

All these conditions lead to the next matrix equation

$$\begin{bmatrix} 1 & 1 & \dots & 1 \\ \lambda_1 & \lambda_2 & \dots & \lambda_8 \\ \dots & \dots & \dots & \dots \\ \lambda_1^7 & \lambda_2^7 & \dots & \lambda_8^7 \end{bmatrix} \begin{bmatrix} X_1 \\ X_2 \\ \dots \\ X_8 \end{bmatrix} = \begin{bmatrix} 0 \\ 0 \\ \dots \\ -a_0^{-1} \end{bmatrix}, \quad (2.18)$$

where $X_i = A_i(x') \exp(\lambda_i x')$ for $i = 1 \div 4$ and $X_i = -A_i(x') \exp(\lambda_i x')$ for $i = 5 \div 8$. Obviously, the matrix from the eq. (2.18) has the Vandermonde determinant and in fact all Cramer's determinants are Vandermonde determinants, as well.

Eq. (2.18) has the following solution

$$X_i = \frac{1}{a_0 \prod_{k \neq i} (\lambda_k - \lambda_i)}, \quad i, k = 1 \div 8 \quad (2.19)$$

and finally, the Green's function of the H operator is obtained

$$\begin{aligned} \Gamma^-(x, x', \omega) &= \frac{1}{a_0} \sum_{i=1}^4 \frac{\exp[\lambda_i(x-x')]}{\prod_{k \neq i} (\lambda_k - \lambda_i)} \quad \text{for } -\infty < x < x', \\ \Gamma^+(x, x', \omega) &= -\frac{1}{a_0} \sum_{i=5}^8 \frac{\exp[\lambda_i(x-x')]}{\prod_{k \neq i} (\lambda_k - \lambda_i)} \quad \text{for } x' < x < \infty. \end{aligned} \quad (2.20)$$

The complex Green function's column vector of the track results from eq. (2.10) and (2.13)

$$\{\mathbf{G}(x, \xi, \omega)\} = \int_{-\infty}^{\infty} \Gamma(x, x', \omega) \mathbf{L}_{x, \omega}^* [\delta(x' - \xi) \quad 0]^T dx' \quad (2.21)$$

and, by calculating the integral, one obtains

$$\begin{cases} G_r(x, \xi, \omega) \\ G_s(x, \xi, \omega) \end{cases} = \left\{ \begin{array}{l} \frac{1}{4EI_r EI_s (\gamma_2^4 - \gamma_1^4)} \sum_{i=1}^2 (-1)^{i-1} (p\gamma_i^4 + r) \frac{\exp(-\gamma_i|x-\xi|) - i \exp(i\gamma_i|x-\xi|)}{\gamma_i^3} \\ \frac{s}{4EI_r EI_s (\gamma_2^4 - \gamma_1^4)} \sum_{i=1}^2 (-1)^{i-1} \frac{\exp(-\gamma_i|x-\xi|) - i \exp(i\gamma_i|x-\xi|)}{\gamma_i^3} \end{array} \right\}, \quad (2.22)$$

where $\gamma_{1,2}$ are the eigenvalues in the first quadrant and

$$p = EI_s, \quad r = k_r + k_s - \omega^2 m_s + i\omega(c_r + c_s), \quad s = k_r + i\omega c_r. \quad (2.23)$$

Performing the inverse Fourier transform applied to the complex track's Green functions, the real Green functions for the track result

$$\{\mathbf{g}(x, \xi, t - \tau)\} = \frac{1}{2\pi} \int_{-\infty}^{\infty} \{\mathbf{G}(x, \xi, t - \tau)\} \exp[i\omega(t - \tau)] d\omega = \frac{2}{\pi} \int_0^{\infty} \text{Re}\{\mathbf{G}(x, \xi, t - \tau)\} \cos[\omega(t - \tau)] d\omega, \quad (2.24)$$

where $i^2 = -1$. The last expression resides from the causal character of the track structure.

The track is considered as an infinite and damped mechanical structure and therefore, the track's Green functions are attenuated in space, time and frequency-domains:

$$\begin{aligned} \lim_{x \rightarrow \pm\infty} \{\mathbf{G}(x, \xi, \omega)\} &= \lim_{\xi \rightarrow \pm\infty} \{\mathbf{G}(x, \xi, \omega)\} = \lim_{\omega \rightarrow \pm\infty} \{\mathbf{G}(x, \xi, \omega)\} = 0, \\ \lim_{x \rightarrow \pm\infty} \{\mathbf{g}(x, \xi, t - \tau)\} &= \lim_{\xi \rightarrow \pm\infty} \{\mathbf{g}(x, \xi, t - \tau)\} = \lim_{t - \tau \rightarrow \infty} \{\mathbf{g}(x, \xi, t - \tau)\} = 0. \end{aligned} \quad (2.25)$$

Beside, the track's Green functions are symmetrical (the Maxwell-Betty principle)

$$\{\mathbf{G}(x, \xi, \omega)\} = \{\mathbf{G}(\xi, x, \omega)\}, \quad \{\mathbf{g}(x, \xi, t - \tau)\} = \{\mathbf{g}(\xi, x, t - \tau)\}. \quad (2.26)$$

The real track's Green functions are calculated by numerical integration using the help of cubic spline functions and their previous properties.

The rail and slab displacement may be determined as

$$\{\mathbf{w}(x, t)\} = \int_{-\infty}^{\infty} \int_0^t \{\mathbf{g}(x, \xi, t - \tau)\} Q(\tau) \delta(\xi - V\tau) d\tau d\xi = \int_0^t \{\mathbf{g}(x, V\tau, t - \tau)\} Q(\tau) d\tau. \quad (2.27)$$

Practically, there is a certain T for which the norm of Green function's is "concentrated" in the $[0, T]$ interval because the track is damped and for any $t > T$, the rail and slab displacement may be computed as

$$\{\mathbf{w}(x, t)\} \equiv \int_{t-T}^t \{\mathbf{g}(x, V\tau, t-\tau)\} Q(\tau) d\tau. \quad (2.28)$$

In order to solve the problem of the wheel/track interaction, the rail displacement at contact point is required

$$w_r(Vt, t) = \int_0^t g_r(Vt, V\tau, t-\tau) Q(\tau) d\tau, \quad (2.29)$$

where $g_r(Vt, V\tau, t-\tau)$ is the Green function for the rail displacement. This means that for any contact point $x = Vt$, there is a corresponding Green function $g_r(Vt, V\tau, t-\tau)$ which depends on $0 \leq \tau \leq t$ and it is calculated from $g_r(x, \xi, t-\tau)$. Eq. (2.29) is general (for any $t > 0$), but for the particular case when $t > T$, only the history for $\tau \in [t-T, t]$ is necessary, according to the attenuation in time-domain. Moreover, all contact points $x = Vt$ with $t > T$ have the same sequence of Green function because the track has the homogeneous structure.

From the numeric integration viewpoint, there are two steps to do. The first one refers to $0 \leq t \leq T$ - the 'transitory' period of numeric integration is, while the second step assumes $T \leq t$, which means the 'stationary' period of numeric integration.

When using the small time-steps method on short Δt time intervals in order to integrate eq. (2.27), the Green function will be calculated in $N = T/\Delta t + 1$ and all the obtained values may be encapsulated in the so-called *track's Green matrix* which depends on speed value V . This matrix includes the required values for the transitory period of numeric integration. Also, it includes the rail's Green vector and starting from this, the wheel/rail displacements and the normal contact force may be computed very simple and fast.

In fact, a time partition - t_0, t_1, \dots, t_n with $t_0 = 0, t_n = t$ and $\Delta t = t_i - t_{i-1}$ where $i = 1 \div n$ - has to be considered. From the equations for the wheel and rail displacement, the recurrent forms are available

$$\begin{aligned} \dot{z}_w(t_n) &= \dot{z}_w(t_{n-1}) + \frac{1}{M_w} \int_{t_{n-1}}^{t_n} [Q_0 - Q(\tau)] d\tau, \quad z_w(t_n) = z_w(t_{n-1}) + \int_{t_{n-1}}^{t_n} \dot{z}_w(\tau) d\tau, \\ w_r(Vt_n, t_n) &= \sum_{i=1}^n \int_{t_{i-1}}^{t_i} g_r(Vt_n, V\tau, t_n - \tau) d\tau. \end{aligned} \quad (2.30)$$

Assuming that in the time interval $[t_{i-1}, t_i]$, the Green functions and the normal contact force $Q(\tau)$ have a linear variation, the previous integrations may be performed

$$\begin{aligned} \dot{z}_w(t_n) &= \dot{z}_w(t_{n-1}) + \frac{\Delta t}{M_w} \left[Q_0 - \frac{Q(t_n) + Q(t_{n-1})}{2} \right], \\ z_w(t_n) &= z_w(t_{n-1}) + z_w(t_{n-1}) \Delta t + \frac{\Delta t^2}{2M_w} \left[Q_0 - \frac{Q(t_n) + 2Q(t_{n-1})}{3} \right], \\ w_r(Vt_n, t_n) &= \Delta t \sum_{i=1}^n \left\{ \frac{g_r(t_{i-1})Q(t_i) + g_r(t_i)Q(t_{i-1})}{2} + \frac{[g_r(t_{i-1}) - g_r(t_{i-1})][Q(t_i) - Q(t_{i-1})]}{3} \right\}, \end{aligned} \quad (2.31)$$

where $g_r(t_i) = g_r(Vt_n, Vt_i, t_n - t_i)$.

As it may be observed, the wheel and rail displacement are depending on the magnitude of normal contact force $Q(t_n)$ and inserting these displacements in the equation of normal contact force (2.5), a nonlinear $Q(t_n)$ based equation reads. Solving this equation in an iterative manner, the normal contact force results and then coming back to eqs. (2.31), the wheel displacement and the rail deflection at contact point are calculated for each integration step. The slab displacement at contact section will be traced in a similar way.

Last question discussed in this chapter is focused on the frequency-domain analysis. To do this analysis, the following equations have to be considered

$$\Delta Q = -\frac{u}{\alpha_w + \alpha_r + \alpha_H}, \quad z_w = \frac{\alpha_w u}{\alpha_w + \alpha_r + \alpha_H}, \quad w_r = -\frac{\alpha_r u}{\alpha_w + \alpha_r + \alpha_H}, \quad (2.32)$$

where α_w is the wheel receptance, $\alpha_r = G_r(Vt, Vt, \omega)$ is the rail receptance at the contact point and $\alpha_H = 1/k_H$ is the contact receptance (k_H is the contact stiffness). All variables are complex values excepting the contact receptance. The rail receptance will be calculated in moving frame because it depends on the wheel velocity.

3. NUMERICAL APPLICATION

In this section, both frequency-domain and time-domain numerical analysis of a particular wheel that uniformly moves along an embedded track is presented. The model parameters for wheel are as following: $M_w = 600$ kg and $Q_0 = 100$ kN. Track's parameters are: $m_r = 60$ kg/m, $EI_r = 6.42$ MNm², $m_s = 1680$ kg/m, $EI_s = 280$ MNm², $k_r = 33$ MN/m², $c_r = 5.0$ kNs/m², $k_s = 66$ MN/m² and $c_s = 30$ kNs/m². The Hertzian constant $C_H = 9.64 \cdot 10^{10}$ N/m^{3/2} is determined taking the curve radiuses of the UIC 60 rail-type and the radius of 0.5 m for the wheel (conic profile). The stiffness of wheel/rail contact has value of 1.46 GN/m.

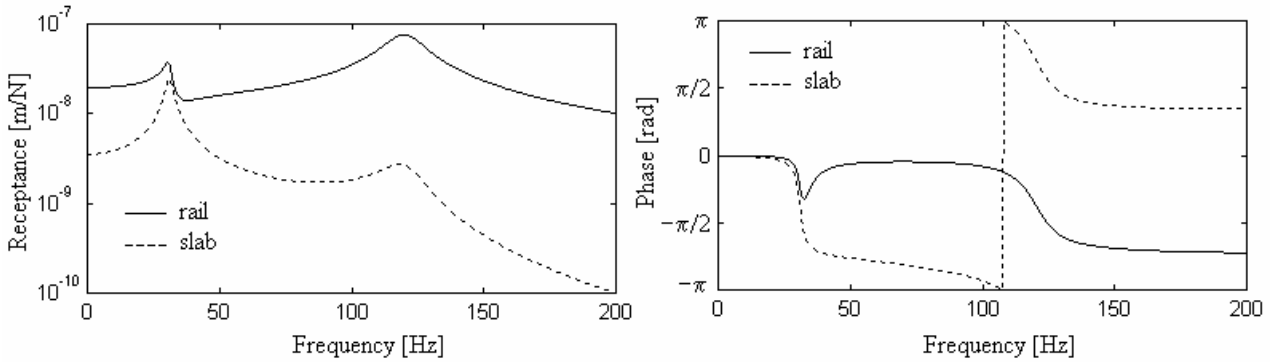


Fig. 3.1.

Fig. 3.1. displays the track's receptances and phases, calculated at the point of a unitary non-moving harmonic excitation. The rail's receptance diagram is very similar with the results from the previous related papers [10, 12]. The response of the track is dominated by two peaks at 31 and 120 Hz because the rail and the slab vibrate as a discrete system with two degrees of freedom. At the first resonance frequency, the rail and the slab are in phase and then, they vibrate in anti-phase. The first peak belongs to the slab resonance, and the second one is produced by the rail's resonance. The rail receptance is significantly higher than the slab receptance due to its low inertia and the elasticity of the rail-pad.

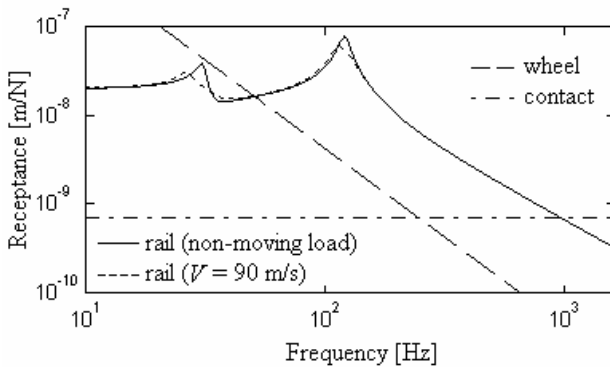


Fig. 3.2.

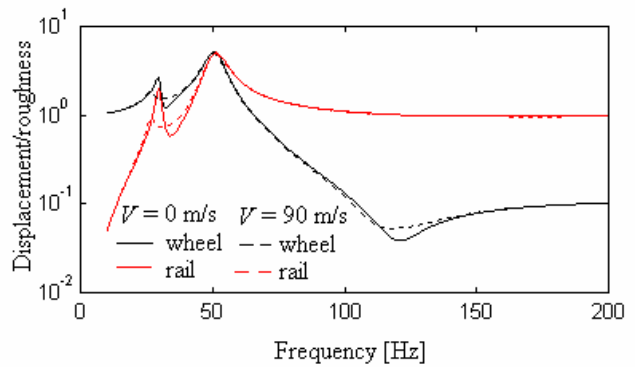


Fig. 3.3.

The wheel/rail system's vertical response is strongly correlated with the receptances of the two bodies and contact elasticity (fig. 3.2.). In the frequency range, the rail receptance is influenced by the velocity of the unitary harmonic excitation only in the two peaks. In fact, the rail's receptance decreases when the velocity increases. The two resonance frequencies decrease as well, especially the lower resonance. The rail and the wheel's receptances meet at a frequency of about 51 Hz. At low frequencies, the wheel receptance is

higher. On the contrary, the rail is more flexible at higher frequencies. The contact elasticity is much lower than the rail receptance, but they meet at higher frequencies, i.e. around 1000 Hz.

The wheel/rail response in frequency-domain of 0-200 Hz is presented in fig. 3.3. The wheel/rail system exhibits two resonance frequencies, corresponding to the structure of the two degrees of freedoms. The first resonance frequency appears around 30 Hz and the second around 51 Hz when the wheel receptance equals the rail receptance as described above. The wheel displacement is higher than the rail's at frequencies below 51 Hz because the wheel receptance is higher in this domain. When passing beyond the second resonance frequency, the rail receptance becomes higher than the wheel's and the rail displacement is higher as well. The wheel response accuses anti-resonance at the resonance frequency of the rail, i.e. 120 Hz, due to its maximum receptance. On the other hand, both rail and wheel responses decrease at the first resonance frequency because the rail is more flexible in case of a moving wheel.

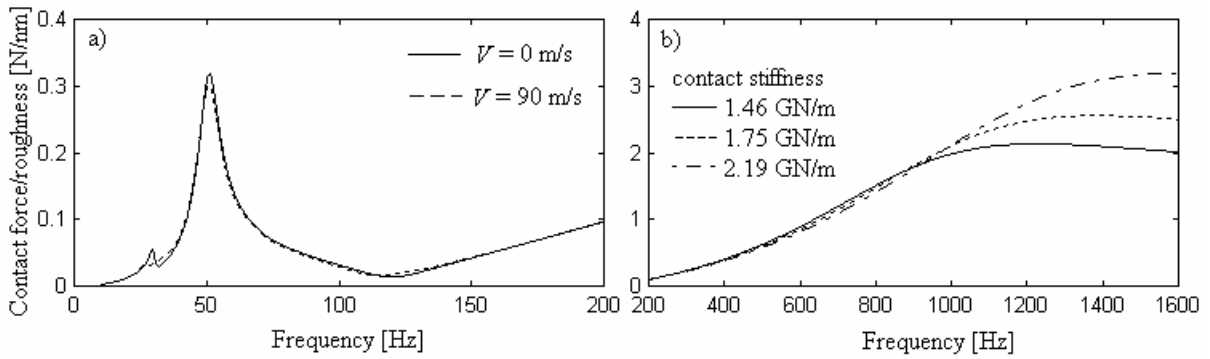


Fig. 3.4.

The wheel/rail contact force is displayed in fig. 3.4. The trend of the contact force has two peaks at the resonance frequencies of the wheel/rail system (fig. 3.4.a). These peaks are barely influenced by the wheel velocity. Beyond this, the contact force decreases while frequency increases and it has the minimum value at the rail's resonance frequency. By gradually increasing the frequency, the contact force increases as well. The contact stiffness is of importance at higher frequencies as it may be seen in fig. 3.4.b. In fact, the rail profile wears out due to the passing wheels and the contact elasticity decreases. As a result, a large contact force appears and influences the wheel/rail behaviour at higher frequencies. More specific, it may be demonstrated that the contact force increases as the contact elasticity decreases for higher frequencies than the approximate value given as

$$f = \left(4\alpha_H \sqrt[4]{EI_r m_r^3} \right)^{-2/3}, \quad (2.33)$$

and the contact force has a contrary trend for lower frequencies. In this particular case, the frequency f has the following values: $f = 770$ Hz for $k_H = 1.46$ GN/m, $f = 867$ Hz for $k_H = 1.75$ GN/m and $f = 1009$ Hz for $k_H = 2.19$ GN/m.

The complex Green functions are used to calculate the track's real Green functions. The integration domain was chosen between 0 and 5 kHz and the integration step was chosen as 2 Hz.

Fig. 3.5. presents the rail's real Green function at unitary impulse point, $g_w(x, x, t)$. In the beginning, the rail response is dominated by the oscillation which has the frequency of 120 Hz (fig. 3.5.a) and then the response exhibits the oscillation from 31 Hz, according to the results from the frequency-domain analysis. The response is slowly damped comparing to the ballasted track [20]. However, after 0,5 s, the response amplitude is less than 1/440 from its root mean square calculated for this period.

Fig. 3.6. shows the rail's response when the unitary impulse point is applied 30 m away. The bending waves have the highest frequency of 5 kHz due to cut-off frequency applied by numerical integration. Every bending wave has its particular group velocity. For this reason, the rail response is delayed and has a proper shape because the bending waves arrive one by one. In fact, the bending wave of 5 kHz arrives first because it has the highest group velocity. Basically, the rail is decoupled from the rail pad for the high frequency range and the group velocity is given as

$$v_g = 2 \cdot 4 \sqrt{\frac{\omega^2 EI_r}{m_r}} \quad (2.33)$$

Starting from this formula, the delay of about 4.7 ms is obtained for the bending wave of 5 kHz, as it may be seen in the detail of the figure.

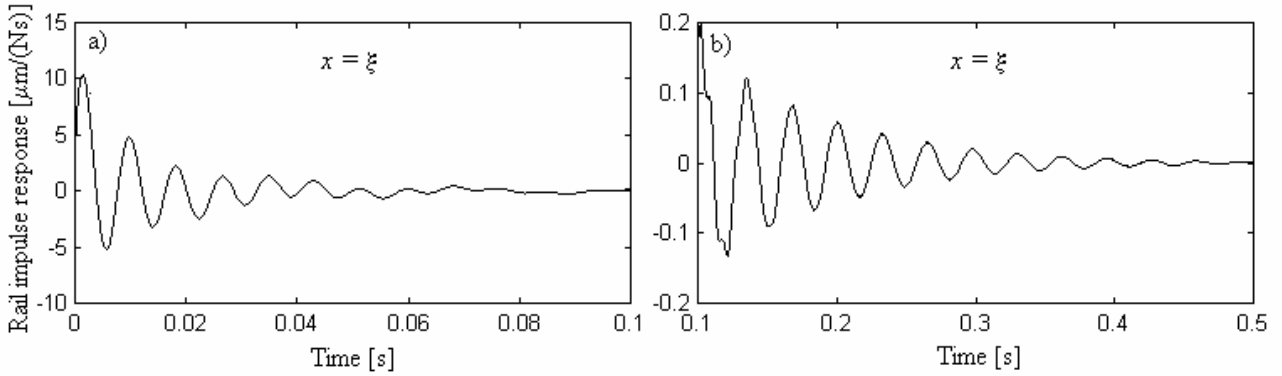


Fig. 3.5.

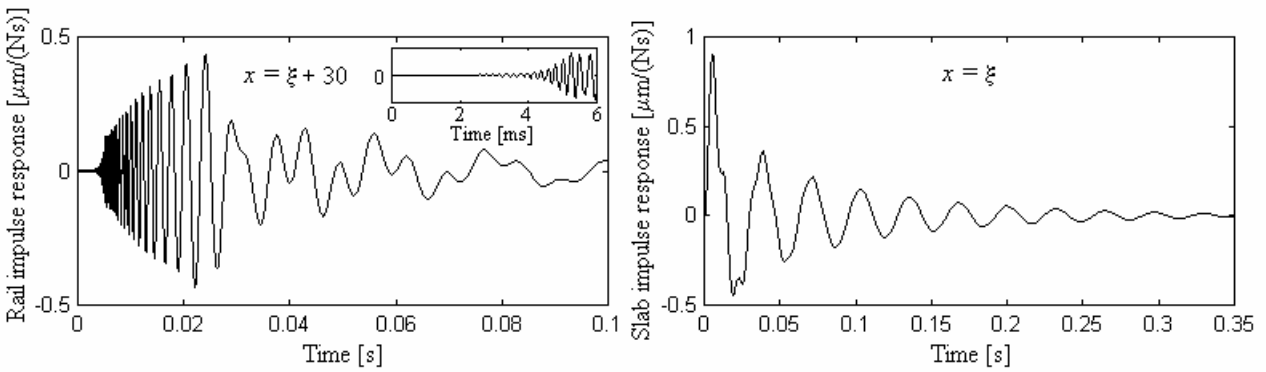


Fig. 3.6.

Fig. 3.7.

Fig. 3.7. displays the slab response under the section of the unitary impulse applied on rail. The response magnitude is lower than the rail's as it may be observed by comparing it to fig. 3.5. Practically, the slab response is dominated by the oscillation which has the frequency of 31 Hz, i.e. the own frequency of slab on its Winkler foundation.

In the following, the real Green functions will be used to simulate the dynamics of a moving wheel on a slab track for different values of wheel speed. According to the previous results, the transitory period of 0.5 s for numeric integration has been chosen. Also, the time step for integrating the equations of motion corresponds to the frequency of 40 kHz which is adequate for capturing the high frequency dynamic response of the wheel/rail system. The real part of the complex Green functions was calculated for the resulting track length (VT) at a higher step and then interpolated with spline functions at small step.

Fig. 3.8. presents the wheel and rail displacements at contact point when the wheel passes at 60 m/s over a rail's manufacturing defect which has the wavelength of 1.6 m and amplitude of 0.1 mm [25]. The wheel displacement is higher than the rail displacement due to the elastic Hertzian contact. The appropriate frequency for this irregularity is 37.5 Hz and the rail receptance is lower than the wheel receptance. As a consequence, the wheel amplitude is higher according to the result from the frequency-domain analysis. On the other hand, the displacement of the slab at contact point section and its amplitude are lower than the rail's. The motion has a strong harmonic character because the stiffness contact effect is minor.

Fig. 3.9. shows the velocity influence on the wheel/rail contact force. The effective contact force follows the same trend as in frequency-domain. It exhibits two relative maximum values corresponding to

the two resonance frequencies, at 46 m/s and 81 m/s respectively, when the passing frequency equals the own wheel/track frequencies.

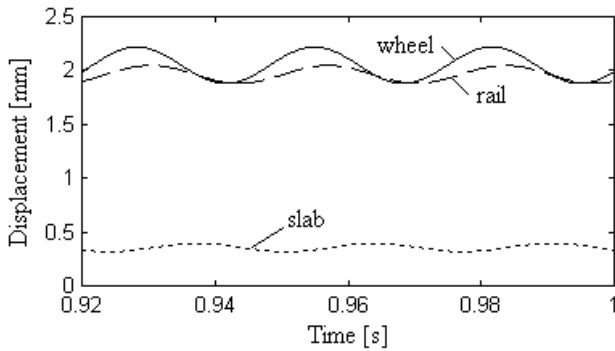


Fig. 3.8.

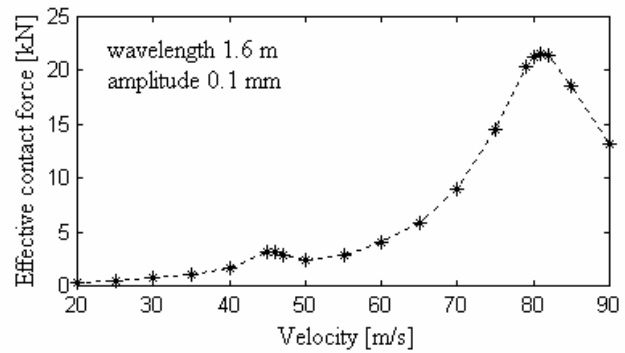


Fig. 3.9.

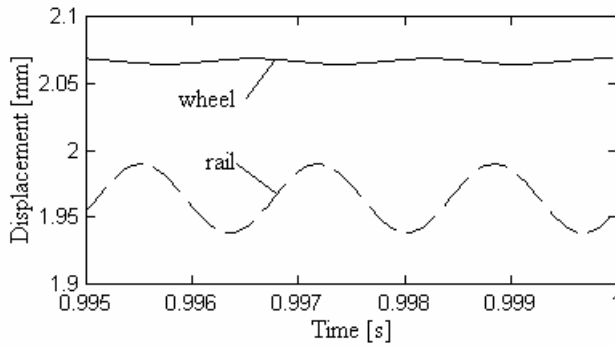


Fig. 3.10.

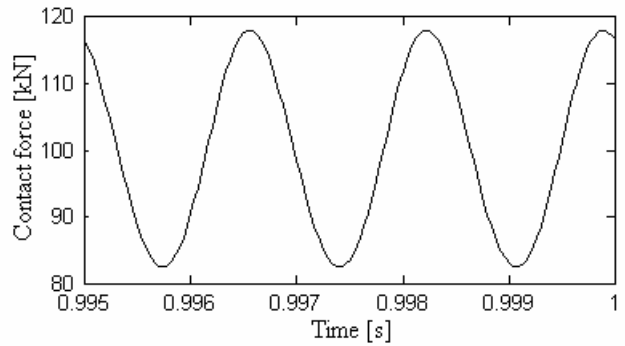


Fig. 3.11.

When the rail is affected by the short corrugation, the excitation frequency of the wheel/rail system takes places in the middle and high range for usual velocities of the modern railway networks. For instance, fig. 3.10 displays the results from the numerical simulation that considers a wheel rolling at 60 m/s over a short corrugation which has wavelength of 100 mm and amplitude of 20 μm . The wheel/rail vibration occurs at the frequency of 600 Hz and the wheel amplitude is significantly lower than the rail amplitude at contact point due to the high wheel inertia.

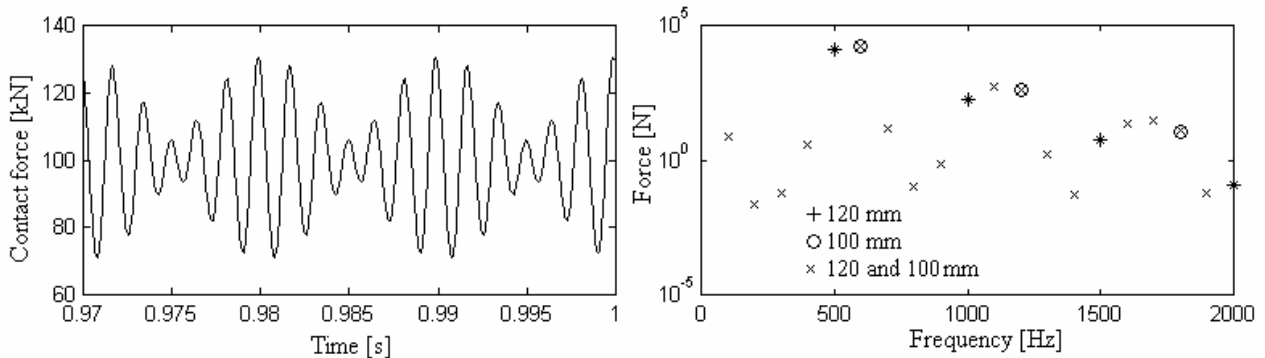


Fig. 3.12.

The time evolution of the contact force is not symmetric around the static load due to nonlinearity of the Hertzian contact (fig. 3.11). Actually, the contact force increases to an amplitude of 17.17 kN and decreases to an amplitude of 16.81 kN. The spectrum of contact force has super-harmonic components and the second harmonic is of significant magnitude comparing to the precedent case.

When the wheel passes over two sinusoidal irregularities, the spectrum exhibits super-harmonic and sub-harmonic components as well. Time history of the contact force and its spectrum are presented in Fig. 3.12. for the case of a moving wheel at 60 m/s over two sinusoidal irregularities which have the same amplitude of 20 μm and the wavelength of 100 and 120 mm respectively. The fundamental components have the frequency of 600 Hz and 500 Hz. The frequencies of super-harmonic components are multiples of the fundamental frequencies. Practically, these super-harmonics are overlapped by the super-harmonics due to a single sinusoidal irregularity corresponding to the wavelength of 100 mm or 120 mm. Also, the spectrum has many sub-harmonic components. It may be observed that the strong super-harmonic components are inserted between super-harmonics of the two fundamental components.

4. CONCLUSIONS

The response of infinite structure consisting of elastically supported double Euler-Bernoulli beams due to a moving wheel in the presence of irregularities of rolling surfaces has been analyzed both in frequency-domain and time-domain. This particular issue is of practical importance for wheel/slab track interaction and to point out the basic features of such a system, a simple mechanical model has been considered.

To this end, an original semi-analytical method based on the outstanding properties of the real Green's functions of the track has been developed for time-domain approach. Actually, these functions were calculated by integrating the complex Green functions and then they were encapsulated in track's Green matrix. The real Green's function of the rail is crucial to solve the interaction problem including the nonlinear wheel/rail contact, for any time period. Also, the Green function method surmounts the difficulties relates by the model edges effect.

The wheel/slab track system has two resonances placed in the low frequencies range. The wheel velocity influences the wheel/rail response in frequency-domain around two resonances only. The contact stiffness is not an important feature in this frequency range.

On contrary, in the middle and high frequency range, the contact stiffness influences the wheel/rail force magnitude. More precisely, the contact force increases as the contact stiffness increases in high frequencies range and it decreases in the mid-frequencies domain. Also, the contact nonlinearity originates sub-harmonic and super-harmonic components which influence the wear process of the rolling surfaces.

REFERENCES

1. REMINGTON, J. P., *Wheel/rail noise – Part I: characterization of the wheel/rail dynamic system*, Journal of Sound and Vibration, **46**, pp. 359-379, 1976.
2. REMINGTON, J. P., *Wheel/rail noise I: theoretical analysis*, Journal of the Acoustical Society of America, **81**, pp. 1805-1823, 1987.
3. THOMPSON, D. J., *Wheel-rail contact noise: development and detailed evaluation of a theoretical model for the generation of wheel and rail vibration due to surface roughness*, ORE DT 204 (C 163), Utrecht, 1988.
4. GRASSIE, S., KALOUSEK, J., *Rail corrugations. Characteristics, causes and treatments*, Institute of Mechanical Engineers, Part F: Journal of Rail and Rapid Transit **207** pp. 57-68, 1993.
5. NIELSEN, J. C. O., LUNDEN, R., JOHANSSON, A., VERNERSSON, T., *Train-Track Interaction and Mechanisms of Irregular Wear on Wheel and Rail Surfaces*, Vehicle System Dynamics, **40**, 1-3, pp. 3-54, 2003.
6. GRASSIE, S. L., GREGORY, R. W., HARRISON, D., JOHNSON, K. L., *The dynamic response of railway track to high frequency vertical excitation*, Journal Mechanical Engineering Science **24**, pp. 77-90, 1982.
7. STEENBERGEN, M. J. M. M., METRIKINE, A. V., ESVELD, C., *Assessment of design parameters of a slab track railway system from a dynamic viewpoint*, Journal of Sound and Vibration **306**, pp. 361-371, 2007.
8. ESVELD, C., *Track structures in an urban environment*, TU Delft, Symposium K.U. Leuven, 21 pages, 1997.
9. SATO, Y., *Study on high-frequency in track operated with high-speed trains*, Quarterly Reports of RTRI **18**, pp. 109-144, 1977.
10. BITZENBAUER, J., DINKEL, J., *Dynamic interaction between a moving vehicle and an infinite structure excited by irregularities - Fourier transforms solution*, Archive of Applied Mechanics **72**, pp. 199-211, 2002.
11. SHAMALTA, M., METRIKINE, A. V., *Analytical study of the dynamic response of an embedded railway track to a moving load*, Archive of Applied Mechanics **73**, pp. 131-146, 2003.
12. HUSSEIN, M. F. M., HUNT, H. E. M., *Modelling of floating-slab tracks with continuous slabs under oscillating moving loads*, Journal of Sound and Vibration, **297**, pp. 37-54, 2006.
13. GRASSIE, S., *Measurement of railhead longitudinal profiles: a comparison of different techniques*, Wear **191** pp. 245-251, 1996.

14. THOMPSON, D. J., van VLIET, W. J., VERHEIJ, J. W., *Developments of the indirect method for measuring the high frequency dynamic stiffness of resilient elements*, Journal of Sound and Vibration **213**, pp. 169-188, 1998.
15. WU, T. X., THOMPSON, D. J., *The effect of local preload on the foundation stiffness and vertical vibration of railway track*, Journal of Sound and Vibration **219**, pp. 881-904, 1999.
16. THOMPSON, D. J., HEMSWORTH, B., VINCENT, N., *Experimental validation of the TWINS prediction program for rolling noise, Part I: description of the model and method*, Journal of Sound and Vibration **193**, pp. 123-135, 1996.
17. HOU, K., KALOUSEK, J., DONG, R. G., *A dynamic model for an asymmetrical vehicle/train system*, Journal of Sound and Vibration **267** pp. 591-604, 2003.
18. WU, T. X., THOMPSON, D. J., *On the parametric excitation of the wheel/track system*, Journal of Sound and Vibration **278**, pp.725-747, 2004.
19. SHENG, X., LI, M., JONES, C. J. C., THOMPSON, D. J., *Using the Fourier-series approach to study interactions between moving wheels and a periodically supported rail*, Journal of Sound and Vibration **303**, pp. 873-894, 2007.
20. MAZILU, Tr., *Green's functions for analysis of dynamic response of wheel-rail to vertical excitation*, Journal of Sound and Vibration, **306**, pp. 31-58, 2007.
21. MAZILU, Tr., *A dynamic model for the impact between the wheel flat and rail*, UPB Scientific Bulletin, Series D: Mechanical Engineering, **69**(2), pp. 45-58, 2007.
22. MAZILU, Tr., *Wheel-rail vibrations* (in Roumanian), MatrixRom, 436 pages, 2008.
23. CREMER, L., HECKL, M., *Structure-Borne Sound Structural Vibrations and Sound Radiation at Audio Frequencies*, Springer-Verlag Berlin, Heidelberg 1973 and 1988.
24. MOCICĂ, Gh. *The Laplace transform and operational methods* (in Roumanian), UPB, 536 pages, 1993.
25. ALIAS, J., *Caractères de l'usure ondulatoire*, Rail International, novembre, pp. 17-23, 1986,

Received November 10, 2008